Characterization of tandem aerosol classifiers for selecting particles: implication for eliminating multiple charging effect

Yao Song[1], Xiangyu Pei[1], Huichao Liu[1], Jiajia Zhou[1], Zhibin Wang[1,2,3*]

[1] College of Environmental and Resource Sciences, Zhejiang Provincial Key Laboratory of Organic Pollution Process and Control, Zhejiang University, Hangzhou, 310058, China
[2] ZJU-Hangzhou Global Scientific and Technological Innovation Center, Hangzhou 311200, China ~~Hangzhou Global Scientific and Technological Innovation Center, Zhejiang University, Hangzhou, 311200, China~~
[3] Key Laboratory of Environment Remediation and Ecological Health, Ministry of Education, Zhejiang University, ~~310058~~ Hangzhou 310058, China

Correspondence to: Zhibin Wang (wangzhibin@zju.edu.cn)

Abstract. Accurate particle classification plays a vital role in aerosol studies. Differential mobility analyzer (DMA), centrifugal particle mass analyzer (CPMA) and aerodynamic aerosol classifier (AAC) are commonly used to select particles with a specific ~~size~~ mobility diameter, aerodynamic diameter or mass, respectively. However, multiple charging effects cannot be entirely avoided when using either individual techniques or tandem systems such as DMA-CPMA, especially when selecting soot particles with fractal structures. In this study, we ~~demonstrate~~ calculate the transfer functions of the DMA-CPMA and DMA-AAC in static configurations for flame generated soot particles. We propose an equation that constrains the resolutions of DMA and CPMA to eliminate the multiple charging effect when selecting particles with a certain mass–mobility relationship using the DMA-CPMA system. The equation for the DMA-AAC system is also derived. For DMA-CPMA in a static configuration, ~~O~~our results show that the ability to remove multiply charged particles mainly depends on the particle morphology and resolution~~s~~ settings of the DMA and CPMA. Using measurements from soot experiments and literature data, a general trend in the appearance of multiple charging effect with decreasing size when selecting aspherical particles is observed. ~~Otherwise~~As for DMA-AAC in a static configuration, ~~our results indicate that~~ the ability ~~of the DMA-AAC in a static configuration~~ to eliminate particles with multiple charges is mainly related to the resolutions of classifiers. In most cases, the DMA-AAC in a static configuration can eliminate multiple charging effect regardless of the particle morphology, but multiply charged particles will be selected when decreasing the resolution of the DMA or AAC. We propose that the potential influence of the multiple charging effect should be considered when using the DMA-CPMA or DMA-AAC systems in estimating size- and mass-resolved optical properties in field and lab experiments.

1 Introduction

Atmospheric aerosol particles span a wide size range from 1 nm to > 100 μm. A significant size dependence of aerosol physicochemical properties has been widely reported. Particle size can strongly alter the hygroscopic behavior (Biskos et al., 2006), phase state (Cheng et al., 2015) and cloud-nucleating ability (Dusek et al., 2006) of aerosol nanoparticles, indicating the importance of particle size when assessing the climate effect. Hence, accurate particle classification is essential when investigating the size ~~dependence~~ dependent behavior of aerosol particles.

At present, particles are generally classified by either size or mass in atmospheric aerosol studies. A differential mobility analyzer (DMA) is the most commonly used size classifier, which selects particles based on electrical mobility (Knutson and Whitby, 1975; Park et al., 2008; Stolzenburg and McMurry, 2008; Swietlicki et al., 2008; Wiedensohler et al., 2012). A particle mass analyzer (PMA) includes an aerosol particle mass analyzer (APM) and a centrifugal particle mass analyzer (CPMA), both of which classify particles based on their mass-to-charge ratio (Ehara et al., 1996; Olfert and Collings, 2005). ~~However,~~ The charge distribution of particles must be known by passing through an neutralizer or similar ~~precharged~~ when classified by ~~a~~ DMA or PMA ~~because DMA and PMA classify particles based on electrical mobility and mass-to-charge ratio, respectively, resulting in~~. However, particles with higher-order charges and identical apparent mobility or mass-to-charge ratio ~~being~~ can be selected simultaneously, which are referred to as the multiple charging effect. This may introduce uncertainty in the subsequent characterization. Radney et al. (2013) demonstrated that although single-charged particles account for the highest number fraction (46.3%) of DMA-classified particles (200 nm), their contributions to the total mass concentration and extinction are insignificant (10.8% and 7.96%, respectively). Thus, the reported extinction of particles with a certain diameter has been greatly overestimated due to the multiple charging effect.

Previous studies (Shiraiwa et al., 2010; Rissler et al., 2013; Johnson et al., 2014; Johnson et al., 2021) tried to utilize the combination of size and mass classifiers, such as DMA-APM or DMA-CPMA systems, to obtain singly charged particles. Theoretically, the ability of a DMA-APM to eliminate multiply charged particles is governed by the particle morphology and setups of the DMA- and APM (Kuwata, 2015). This conclusion implies that multiply charged particles cannot be effectively excluded for aspherical particles, especially for soot particles. Radney and Zangmeister (2016) investigated the limitations of a DMA-APM with three types of particles (polystyrene latex (PSL) spheres, ammonium sulfate (AS) and soot particles). Their results demonstrated that a DMA-APM can resolve multiply charged particles for spherical particles (PSL and AS particles), but it failed for aspherical soot particles. Multiply charged soot particles led to over 110% errors in retrieving the mass specific extinction cross section.

In contrast to DMA and PMA, an aerodynamic aerosol classifier (AAC) is a novel instrument that selects the aerodynamic equivalent diameter of aerosol particles based on their relaxation time. The advantage of utilizing an AAC is that the charge state of the particles does not need to be known ~~no charging process is needed~~ in particle classification compared with the aforementioned classifiers; hence, multiple charging

2

69 effects can be avoided (Tavakoli and Olfert, 2013). However, the selected particles are not monodispersed in

70 mobility diameter when an AAC is used to select aspherical particles (Kazemimanesh et al., 2022).

71 Morphology information, such as effective density (ρ_{eff}), mass–mobility exponent (D_{fm}) and dynamic shape

72 factor (χ), can be inferred using tandem DMA-PMA system (Park et al., 2003; Zhang et al., 2008; Rissler et

73 al., 2013; Pei et al., 2018; Zangmeister et al., 2018), DMA-AAC (Tavakoli and Olfert, 2014) and AAC-

74 CPMA systems (Kazemimanesh et al., 2022Johnson et al., 2018). The derived ρ_{eff} and χ depend upon the

75 combination of instruments used, while the nonphysical values of χ and ρ_{eff} for aspherical particles can be

76 determined by the AAC-APM (Yao et al., 2020) and AAC-CPMA (Kazemimanesh et al., 2022).

77 The theoretical transfer functions of individual classifiers (DMA, CPMA and AAC) and the DMA-APM

78 system have been previously discussed (Knutson and Whitby, 1975; Ehara et al., 1996; Olfert and Collings,

79 2005; Stolzenburg and McMurry, 2008; Tavakoli and Olfert, 2013). In this study, we focus on a DMA-

80 CPMA and DMA-AAC in static configurations to eliminate multiply charged particles. The DMA-CPMA

81 and DMA-AAC systems mentioned below refer to the tandems of a DMA and CPMA or a DMA and AAC

82 in a static configuration, respectively. We calculate the transfer functions of the DMA-AAC and DMA-

83 CPMA systematically. Combined with soot experiments, we demonstrate that multiple charging effects may

84 still exist after DMA-CPMA classification when selecting aspherical particles and evaluate the light

85 absorption of selected particles with different charging states using Mie theory. Furthermore, we propose

86 operating conditions for the DMA-CPMA and DMA-AAC to eliminate multiply charged particles in future

87 studies. Our results suggest that the size- and mass-resolved optical properties may be overestimated for

88 small soot particles when using the DMA-CPMA system, which will lower the prediction accuracy of the

89 fresh soot climate effect. In Sect. 3.1, we calculate the transfer functions of the DMA-CPMA and DMA-

90 AAC utilizing the literature data of soot particles from Pei et al. (2018). In Sect. 3.2, we measure the multiple

91 charging effect of the DMA-CPMA using laboratory-generated soot particles, and the bias of optical

92 measurement induced by multiply charged particles is evaluated in Sect. 3.3.

93 **2 Theory and experiment**

94 **2.1 Transfer function for individual aerosol classifiers**

95 **DMA**

96 The DMA, consisting of two coaxial electrodes, classifies particles based upon electrical mobility Z_{p}

97 (Knutson and Whitby, 1975), which can be calculated as follows:

98 $Z_{\text{p}} = q\text{B} = \frac{neCc(d_{\text{m}})}{3\pi\mu d_{\text{m}}}$,   (1)

99 where q is the particle charge, n is the number of elementary charges, B is the mobility of the particle, e is

100 the elementary charge, μ is the viscosity of air, and $Cc(d_{\text{p}})$ is the Cunningham slip correction factor. When

101 the aerosol inlet flow rate equals the aerosol sampling outlet flow rate, the centroid mobility, $Z_{\text{p}}^{*}Z_{\text{p}}^{*}$ selected

102 by the DMA is defined as

3

103    $$Z_{\mathrm{p}}^{*} = \frac{Q_{\mathrm{sh}}}{2\pi V_{\mathrm{DMA}}L_{\mathrm{DMA}}}\ln\left(\frac{r_{2\_\mathrm{DMA}}}{r_{1\_\mathrm{DMA}}}\right),$$ (2)

104   where Q_{sh} is the sheath flow rate, V_{DMA} is the voltage between the two electrodes, L_{DMA} is the length of the

105   DMA, and r_{1_DMA} and r_{2_DMA} are the inner and outer radii of the DMA electrodes, respectively. Assuming

106   that the aerosol inlet and aerosol sampling flow rates are equal, the transfer function of the DMA can be

107   expressed as follows when particle diffusion is negligible (Knutson and Whitby, 1975; Stolzenburg and

108   McMurry, 2008):

109    $$\Omega\left(\tilde{Z}_{\mathrm{p}}, \beta_{\mathrm{DMA}}\right) = \frac{1}{2\beta_{\mathrm{DMA}}}\left[\left|\tilde{Z}_{\mathrm{p}} - (1 + \beta_{\mathrm{DMA}})\right| + \left|\tilde{Z}_{\mathrm{p}} - (1 - \beta_{\mathrm{DMA}})\right| - 2\left|\tilde{Z}_{\mathrm{p}} - 1\right|\right],$$ (3)

110   where, $\tilde{Z}_{\mathrm{p}} = Z_{\mathrm{p}}/Z_{\mathrm{p}}^{*}$, $\beta_{\mathrm{DMA}} = Q_{\mathrm{a}}/Q_{\mathrm{sh}}$, and Q_{a} is the sample flow rate. The limiting electrical mobilities that DMA

111   can select are $(1 \pm \beta_{\mathrm{DMA}})\cdot Z_{\mathrm{p}}^{*}$. The maximum and minimum values of d_{m} for particles with n charges can be

112   derived <u>combining $(1 \pm \beta_{\mathrm{DMA}})\cdot Z_{\mathrm{p}}^{*}$ and Eq. (1),</u> and denote as $d_{\mathrm{m\_n,max}}$ and ~~d_{m}~~ $d_{\mathrm{m\_n,min}}$, respectively. The transfer

113   function is an isosceles triangle with value of 1 at Z_{p}^{*} and going to 0 at $(1 \pm \beta_{\mathrm{DMA}})\cdot Z_{\mathrm{p}}^{*}$. It translates to

114   asymmetry in d_{m} since the relationship between d_{m} and Z_{p} is nonlinear.

115   **CPMA**

116   <u>The APM consists of two coaxial electrodes which are rotating at an equal angular velocity and a voltage is</u>

117   <u>applied between these electrodes to create an electrostatic field (Ehara et al., 1996).</u> The construction of the

118   CPMA is similar to the APM, but its inner cylinder rotates faster than the outer cylinder to create a stable

119   system of forces (Olfert and Collings, 2005). In the CPMA, the equation of particle motion is expressed as

120    $$\frac{m}{\tau}\frac{dr}{dt} = \frac{mv_{\theta}(r)^{2}}{r} - \frac{qV_{\mathrm{CPMA}}}{r\ln\left(\frac{r_{2\_\mathrm{CPMA}}}{r_{1\_\mathrm{CPMA}}}\right)},$$ (4)

121   and the trajectory equation is

122    $$\frac{dr}{dz} = \frac{dr}{dt}\left(\frac{dz}{dt}\right)^{-1} = \frac{c_{r}}{v_{z}},$$ (5)

123   where τ is the relaxation time, m is the mass of the particle, t is time, V is the voltage difference between the

124   two electrodes, and r_{1_CPMA} and r_{2_CPMA} are the radii of the inner and outer electrodes, respectively. c_{r} is the

125   particle migration velocity, v_{z} is the axial flow distribution and v_{θ} is the velocity profile in the angular

126   direction,

127    $$v_{\theta} = \omega_{1}\frac{\hat{r}^{2} - \hat{\omega}}{\hat{r}^{2} - 1}r + \omega_{1}r_{1\_\mathrm{CPMA}}^{2}\frac{\hat{\omega} - 1}{\hat{r}^{2} - 1}\frac{1}{r} = \alpha r + \frac{\beta}{r},$$ (6)

128   where $\hat{\omega} = \omega_{2}/\omega_{1}$ is the ratio of the rotational speed of the outer electrode to the inner electrode and ω_{1} and

129   ω_{2} are the rotational speeds of the inner and outer electrodes, respectively. $\hat{r}$ is the ratio of the inner and outer

130   radii. α and β are the azimuthal flow velocity distribution parameters.

131   Sipkens et al. (2019) presented methods to calculate the transfer function of the CPMA. They considered the

132   Taylor series expansion about the center of the gap $(r_{\mathrm{c}} = (r_{2\_\mathrm{CPMA}} + r_{1\_\mathrm{CPMA}})/2)$ instead of the equilibrium radius

133   to avoid problems with the scenario in which the equilibrium radius does not exist. This method is much

134   simpler and more robust. In this case, the particle migration velocity in the radial direction is

135    $$c_{r} \approx C_{3} + C_{4}(r - r_{\mathrm{c}}),$$ (7)

136   where

137 $$C_3 = \tau \left(\alpha^2 r_\text{c} + \frac{2\alpha\beta}{r_c} + \frac{\beta^2}{r_c^3} - \frac{C_0}{mr_c} \right),$$ (8)

138 $$C_4 = \tau \left(\alpha^2 - \frac{2\alpha\beta}{r_c} - \frac{3\beta^2}{r_c^4} + \frac{C_0}{mr_c^2} \right),$$ (9)

139 $$C_0 = \frac{qV_\text{CPMA}}{\ln(r_{2\_\text{CPMA}}/r_{1\_\text{CPMA}})},$$ (10)

140 Assuming plug flow, the transfer function would be

141 $$\Omega = \frac{r_b - r_a}{2\delta},$$ (11)

142 where $\delta = (r_{2\_\text{CPMA}} - r_{1\_\text{CPMA}})/2$ is the half width of the gap between the two electrodes, and

143 $$r_\text{a} = \min\left\{ r_{2\_\text{CPMA}}, \max\{r_{1\_\text{CPMA}}, G_0(r_{1\_\text{CPMA}})\} \right\},$$ (12)

144 $$r_\text{b} = \min\left\{ r_{2\_\text{CPMA}}, \max\{r_{1\_\text{CPMA}}, G_0(r_{2\_\text{CPMA}})\} \right\},$$ (13)

145 $$G_0(r_\text{L}) = r_\text{c} + \left(r_\text{L} - r_\text{c} + \frac{C_3}{C_4} \right)\exp(-C_4 L\bar{v}) - \frac{C_3}{C_4},$$ (14)

146 where $G_0(r)$ is the operator used to map the final radial position of the particle to its position at the inlet and

147 $\bar{v}$ is the average flow velocity. min{} and max{} are the minimum and maximum values of the quantities in

148 the brackets, respectively.

149 Reavell et al. (2011) calculated the resolution of the CPMA assuming that the gap between two electrodes is

150 narrow enough that the variation of force in the gap can be ignored. The mass resolution (R_m) of CPMA is

151 related to particles mobility. When selecting the particles with mass of m_1 and mobility of B_1, the R_m can be

152 calculated by

153 $$R_\text{m} = \frac{2\pi B_1 L_\text{CPMA} r_c^2 \omega^2 m_1}{Q_\text{CPMA}}.$$ (15)

154 where ω is the equivalent rotational speed calculated by $\omega = \alpha + \frac{\beta}{r_c^2}$, m_1 is the nominal mass that the CPMA

155 can select. Q_CPMA is the volumetric flow rate. The limiting mass can be calculated by

156 $$m_\text{n,min}^\text{n,max} = \text{n} \cdot m_1 \pm \frac{Q_\text{CPMA}}{2\pi B_\text{n,min}^\text{n,max} L_\text{CPMA} r_c^2 \omega^2} = \text{n} \cdot m_1 \pm \frac{m_1}{R_\text{m}} \cdot \frac{B_1}{B_\text{n,min}^\text{n,max}},$$

157 (16)

158 ~~where ω is the equivalent rotational speed calculated by $\omega = \alpha + \frac{\beta}{r_c^2}$, m_1 is the nominal mass that the CPMA~~

159 ~~can select, and~~ where $m_\text{n,min}^\text{n,max}$ and $B_\text{n,min}^\text{n,max}$ are the maximum and minimum mass and corresponding mobility

160 of particles bearing number of elementary charges of n that the CPMA can select, respectively. Further details

161 can be found in Reavell et al. (2011) and Sipkens et al. (2019).

162 **AAC**

163 The AAC classifies particles based on relaxation time, which is defined by

164 $$\tau = Bm = \frac{Cc(d_\text{ae})\rho_0 d_\text{ae}^2}{18\mu},$$ (17)

165 where μ is the viscosity of air. $Cc(d_\text{ae})$ is the slip correction factor. ρ_0 is the standard density with a value of 1

166 g/cm³ (Johnson et al. 2018). When the aerosol inlet flow rate equals the aerosol sampling outlet flow rate, it

167 can be expressed as (Tavakoli and Olfert, 2013)

5

168 $$\Omega = \frac{1}{2\beta_{\text{AAC}}}\left[|\tilde{\tau} - (1 - \beta_{\text{AAC}})| + |\tilde{\tau} - (1 + \beta_{\text{AAC}})| - 2|\tilde{\tau} - 1|\right],$$ (~~17~~18)

169 τ^* is the nominal relaxation time, which is classified by the AAC,

170 $$\tau^* = \frac{2Q_{\text{sh}}}{\pi\omega^2(r_{1\_\text{AAC}}+r_{2\_\text{AAC}})^2 L},$$

171 (~~18~~19)

172 where $\beta_{\text{AAC}} = \frac{Q_a}{Q_{\text{sh}}}$, $\tilde{\tau} = \frac{\tau}{\tau^*}$, r_{1_AAC} and r_{2_AAC} are the inner and outer radii of the AAC, respectively. The

173 limiting τ that AAC can select are $(1 \pm \beta_{\text{AAC}})\cdot \tau^*$. The maximum and minimum values of d_{ae} can be derived

174 and denoted as $d_{\text{ae,max}}$ and $d_{\text{ae,min}}$, respectively.

2.2 Experimental setup

176 A schematic of the experimental setup is illustrated in Fig. 1. Soot particles were generated by a miniature

177 inverted soot generator (Argonaut Scientific Ltd., Canada) with a propane flow of 74.8 SCPM (standard mL

178 per minute, flow in mL min^{-1} converted from ambient to T =298.15 K and P = 101.325 kPa) and an air flow

179 rate of 12 SLPM (Standard L per minute, flow in L min^{-1} converted from ambient to T =298.15 K and P =

180 101.325 kPa). Although this operation setting is not in the open-tip flame regime, the flame is open-tip

181 consistent with Fig. 2d in Moallemi et al. (2019). Detailed aerosol generation methods can be found in

182 Kazemimanesh et al. (2019b) and Moallemi et al. (2019). The polydispersed aerosols were dried to a relative

183 humidity of <20% by a silica dryer and then passed through a soft X-ray neutralizer (Model 3088, TSI, Inc.,

184 USA). Five mobility diameters (80 nm, 100 nm, 150 nm, 200 nm and 250 nm) of soot particles were selected

185 with the DMA (Model 3081, TSI Inc., USA, $\beta_{\text{DMA}} = Q_{\text{sh}}/Q_a = 10$). For the soot characterization, the ~~flow of~~

186 ~~aerosol which is monodispersed in Z_p, monodisperse~~mobility-selected aerosol flow was switched between

187 two parallel lines and fed into the CPMA (Cambustion Ltd., UK) and AAC (Cambustion, Ltd., UK, β_{AAC}

188 $= Q_{\text{sh}}/Q_a = 10$); meanwhile, the condensation particle counter (CPC, Model 3756, TSI, Inc., USA, 0.3 L min^{-1}

189) was switched between the CPMA and AAC. The distributions of particle number concentration as a

190 function of particle mass (m) and aerodynamic diameter (d_{ae}) were ~~determined~~ measured by the scanning

191 mode of the CPMA and AAC, respectively, while the CPC recorded their corresponding number

192 concentrations at each setpoint. For each d_{m}, the m and d_{ae} distributions were measured three times. Between

193 measurements of each d_{m}, the CPC was used behind the DMA, and the number size distribution of the

194 generated soot particles was measured by a scanning mobility particle sizer (SMPS) to ensure ~~that~~ the number

195 size distribution of generated soot particles did not change during the whole experiment. The m and d_{ae}

196 distributions were fitted to log-normal distributions; thus, the mod~~ales~~ values denoted as m_c and $d_{\text{ae},c}$ for the

197 mobility-selected particles were determined. The equation of log-normal distribution used in this study is

198 expressed as

199
$$\begin{cases} N(m) = \frac{N_0}{\sqrt{2\pi}\ln\sigma_m}\exp\left(\frac{-(\log(m)-\log(m_c))^2}{2(\ln\sigma_m)^2}\right) \\ N(d_{\text{ae}}) = \frac{N_0}{\sqrt{2\pi}\ln\sigma_{\text{ae}}}\exp\left(\frac{-(\log(d_{\text{ae}})-\log(d_{\text{ae},c}))^2}{2(\ln\sigma_{\text{ae}})^2}\right) \end{cases}$$
~~$N(m) = \frac{N_0}{\sqrt{2\pi}\ln\sigma_m}\exp\left(\frac{-(\log(m)-\log(m_c))^2}{2(\ln\sigma_m)^2}\right)$~~

$$N(d_{ae}, d_p, x) = \frac{N_0}{\sqrt{2\pi}\ln\sigma_{ae}\sigma} \exp\left(\frac{-(\log n(d_{ae} \times d_p) - \log n(d_{ae,c}\mu))^2}{2(\ln\sigma_{ae}\sigma)^2}\right),$$

(~~19~~20)

where σ_m and σ_{ae} ~~is~~are the geometric standard deviations of m and d_{ae} distributions, respectively. ~~and μ m_c~~ and $d_{ae,c}$ ~~is~~are the geometric mean of m_c ~~or~~and $d_{ae,c}$. ~~σ and μ are fitted from m or d_{ae} distributions~~, respectively. The CPMA and AAC were calibrated with certified PSL spheres (Thermo, USA) with sizes of 70 nm, 150 nm and 303 nm before the measurement. The measured m and d_{ae} were compared to m_{PSL} and $d_{ae, PSL}$, which were calculated with the nominal diameter and density of PSL (1050 kg m^{-3}). The deviations between measured m and m_{PSL} or measured d_{ae} and $d_{ae, PSL}$ were 2.75% and 5.14%, respectively. To quantify the multiple charging effect of particles selected by the DMA-CPMA system, the soot particles were initially selected by the DMA-CPMA at different d_m and the corresponding m. Then, the d_{ae} distribution of mobility and mass selected particles was obtained by stepping the AAC rotation speed of the cylinder with simultaneous measurement of the particle concentration at the AAC outlet using a CPC (Fig. 1b).

3 Results and discussion

3.1 Transfer function of the tandem system

The DMA, PMA and AAC select particles based on the electrical mobility diameter, mass and aerodynamic diameter, respectively. These properties can be connected as follows (Decarlo et al. 2004):

$$\frac{Cc(d_{ae})\rho_0 d_{ae}^2}{6} = \frac{Cc(d_m)\rho_{eff} d_m^2}{6} = m\frac{Cc(d_m)}{\pi d_m},$$

(~~20~~21)

where $\rho_{eff} = \frac{6m}{\pi d_m^3}$. The transfer function of the DMA-APM has been well documented and can be found in Kuwata (2015). The convolution of the transfer functions of the DMA-CPMA and DMA-AAC were calculated by the following equations.

$$\Phi_{DMA-CPMA} = \Omega_{CPMA}\Omega_{DMA},$$

(~~21~~22)

$$\Phi_{DMA-AAC} = \Omega_{DMA}\Omega_{AAC},$$

(~~22~~23)

where Φ and Ω are the transfer functions of the combined and individual classification systems expressed by subscripts, respectively ~~each classification system expressed by subscripts~~. In the following discussion, we explain the transfer functions of the DMA-CPMA and DMA-AAC utilizing the literature data of soot particles (Pei et al., 2018). The d_m and m of the representative particles are 100 nm and 0.33 fg, respectively, and the corresponding d_{ae} is 68.3 nm according to Eq. (~~20~~21). In the calculation, the following parameter set was employed: $d_m =$ ~~80~~ 100 nm, $Q_{DMA} = 0.3$ L min^{-1}, $\beta_{DMA} = 0.1$, $m = 0.$~~16~~ 33 fg, $Q_{CPMA} = 0.3$ L min^{-1}, $R_m = 8$, $d_{ae} = 68.3$ nm, $Q_{AAC} = 0.3$ L min^{-1}, $\beta_{AAC} = 0.1$. The transfer functions of DMA-CPMA and DMA-AAC were solved iteratively using logarithmically spaced d_m, m and d_{ae}, which included 600 points~~, respectively~~ each. The ranges of d_m, m and d_{ae} used in the calculations were from ~~<~~0.8 times of $d_{m1,min}$ to ~~>~~1.2 times of $d_{m2,max}$, and from 0.8 times of ~~<~~$m_{1,min}$ to 1.2 times of ~~>~~$m_{2,max}$, from 0.8 times of ~~<~~$d_{ae,min}$ to 1.2 times of ~~>~~$d_{ae,max}$, respectively. The dimensions of the individual classifiers are summarized in Table 1.

7

DMA-CPMA

The DMA-CPMA transfer function ($\Phi_{\text{DMA-CPMA}}$) for particles mentioned above, i.e. particles with d_{m} of 100 nm and m of 0.33 fg, is calculated in $\log(d_{\text{m}})$-$\log(m)$ space, as shown in Fig. 2. The particles are shown in Fig. 2 in actual d_{m} and m, but when we calculate the resolution of DMA and CPMA, the mobility and effective mass are used. The resolution of CPMA can be calculated by Eq. (15), where m_1 is the mass of singly charged particles which can be selected by the CPMA, i.e. effective mass. In $\log(d_{\text{m}})$-$\log(m)$ space, the mass–mobility relationship is

$$m = k_{\text{f}}(d_{\text{m}}/\text{nm})^{D_{\text{fm}}} , \tag{24}$$

$$\log(m) = D_{\text{fm}}\log(d_{\text{m}}/\text{nm}) + \log(k_{\text{f}}) , \tag{25}$$

In general, D_{fm} equals 3 for spherical particles and smaller than 3 for aspherical particles, although D_{fm} can be larger than 3 for particles that are non-spherical at small d_{m} and approach spherical as d_{m} increases. In the $\log(d_{\text{m}})$-$\log(m)$ space, the relationship of m and d_{m} is linear, with the slope expressed as the mass–mobility exponent (D_{fm}) and the intercept representing the pre-exponential factor (k_{f}). Under this specific operation condition, no overlap was observed between the spherical particle population (black line) and the classification region (the colored blocks) for doubly charged particles, implying that only the singly charged particles were selected. For aspherical particles with $D_{\text{fm}} < 3$, such as soot particles with aggregate structures, the particle population may overlap the doubly charged region when the slope (D_{fm}) is small enough; however, the combination of DMA and CPMA is generally used to avoid the multiple charge effect in soot studies. The reported D_{fm} values are typically in the range of 2.2–2.4 for fresh soot particles (Rissler et al., 2013) and diesel soot particles (Park et al., 2003). In the exemplary case (Pei et al., 2018), the derived D_{fm} of premixed flame-generated soot particles was 2.28, resulting in the particles population always going through the transfer area of doubly charged particles. This implies that the performance of the DMA-CPMA to eliminate multiply charged particles to a certain extent depends on the particle morphology.

The DMA-CPMA system can eliminate the multiply charged particles only if the D_{fm} of the particles is larger than the slope of a line connecting $(d_{\text{m}}, m) = (d_{\text{m2,min}}, m_{\text{2,max}})(d_{\text{m1}}, m_1)$ (as PP_0 shown in Fig. 2). Since the CPMA is used downstream of the DMA, ~~the value of the mass limit of particles with a certain mobility of B can be expressed as follows according to Eq. (15).~~

$$m_{n,\text{min}}^{n,\text{max}} = n \cdot m_1 \pm \frac{Q_{\text{CPMA}}}{2\pi B L_{\text{CPMA}} r_c^2 \omega^2} , \tag{25}$$

~~where $m_{n,\text{min}}^{n,\text{max}}$ is the maximum or minimum particle mass of particles with the mobility of B that would be selected by the CPMA. The subscript n is the charge quantity~~ $m_{\text{2,max}}$ at the d_{m} of $d_{\text{m2,min}}$ can be calculated using Eq. (16) with the known mobility. Accordingly, the ideal condition under static operation to completely eliminate the multiply charged particles is

$$D_{\text{fm}} > PP_0 = \frac{\log(m_{\text{2,max}}/m_1)}{\log(d_{\text{m2,min}}/d_{\text{m1}})} = \frac{\log\left(2 + \frac{2}{R_{\text{m}}(1+\beta_{\text{DMA}})}\right)}{\log\left(\frac{2}{(1+\beta_{\text{DMA}})}\frac{Cc(d_{\text{m2,min}})}{Cc(d_{\text{m1}})}\right)} \tag{26}$$

The ability of the DMA-CPMA to eliminate multiply charged particles depends on the selected d_{m}, m and resolutions of both the DMA and CPMA. Combining Eq. (16), Equation (26) gives instructions in actual

8

268 operation to eliminate multiply charged particles. When selecting particles of certain d_m and m, by decreasing

269 Q_{CPMA}, or increasing ω and β_{DMA}, i.e., by increasing the resolution of the measurement, the potential of

270 multiply charged particles is reduced. Thus, the key to evaluating whether there is a multiple charging effect

271 lies in the particle morphology (D_{fm}) and the slope of PP_0 ~~derived from the actual condition~~calculated from

272 Eq. (26) theoretically. ~~Compared with the DMA-CPMA, the selection of the DMA-APM is more susceptible~~

273 ~~to multiple charging effect. According to the theoretical calculation described in Kuwata (2015), the slope of~~

274 ~~PP_0 of 3.55 was derived when the DMA-APM selects the same example soot particles from Pei et al. (2018)~~

275 ~~(d_m of 100 nm and m of 0.33 fg) with a D_{fm} of 2.28, indicating that the DMA-APM is more subject to the~~

276 ~~multiple charging effect.~~

277 In addition to the instrument setup, the particle morphology is also crucial for the DMA-CPMA. Here, we

278 simulate the critical slope of PP_0 when selecting different d_m and m under the common selecting conditions

279 ($\beta_{DMA} = 0.1$, $Q_{CPMA}=0.3$ L min^{-1}, $R_m = 8$) using Eq. (26), which is represented as contour lines in Fig. 3 (A

280 black and white version is shown as Fig. S4)~~.~~. Under these selection conditions, the DMA-CPMA can select

281 monodispersed particles when the D_{fm} of the particles is larger than the critical slope of PP_0. When selecting

282 small aspherical particles or particles with extremely low density, the critical slope of PP_0 is relatively higher,

283 and the DMA-CPMA classification is sensitive to multiple charging effect. As shown in Fig. 3, d_m, m and

284 the corresponding D_{fm} were taken from the literature (Park et al., 2003; Rissler et al., 2013; Tavakoli et al.,

285 2014; Ait Ali Yahia et al., 2017; Dastanpour et al., 2017; Forestieri et al., 2018; Pei et al., 2018;

286 Kazemimanesh et al., 2019a). Generally, for soot particles with D_{fm} of 2.2-2.4, the multiple charging effect

287 can be avoided for the DMA-CPMA when selecting soot particles with mobility diameters larger than 200

288 nm, while it fails to eliminate multiply charged particles when selecting small soot particles, as shown by the

289 circles and squares in Fig. 3. These potential uncertainties are discussed in detail with flame-generated soot

290 particles in Sect. 3.2.

291 **DMA-AAC**

292 The advantage of the AAC versus the CPMA is that there is no need for a neutralizer to charge aerosol

293 particles to a known charge state. Measuring solely with an AAC will avoid multiple charging. However,

294 aspherical particles with different mass can be selected by the AAC as having identical aerodynamic diameter

295 ~~cannot constrain the properties of aspherical particles as monodisperse as DMA or CPMA classification~~

296 (Kazemimanesh et al., 2022). According to Eq. (2~~0~~1), the population selected by AAC has one physical size

297 (d_{ae}) but the d_m range of this population is wide since soot particles have different densities. Multiple charging

298 becomes a problem when the tandem measurement is made with a DMA or PMA. ~~The transfer function of~~

299 ~~the DMA-AAC selecting the same representative particles was calculated and is shown in log(d_{ae})-log(d_m)~~

300 ~~(Fig. 4a). Moreover, a~~According to Eq. (2~~0~~21) and Eq. (2~~3~~24), the relationship of d_{ae} and d_m of aspherical

301 particles can be expressed as follows:

302 $\log(d_{ae}) = \frac{1}{2}(D_{fm}-1)\log(d_m) + \frac{1}{2}\log\left(\frac{6}{\pi}\frac{Cc(d_m)k_f}{Cc(d_{ae})\rho_0} \cdot 10^{9D_{fm}-18}\right)$, (27)

303 which indicates that the relationship between d_{ae} and d_m is nonlinear since $Cc(d_m)$ and $Cc(d_{ae})$ vary with d_m

304 and d_{ae}, respectively. Particle morphology can be derived from the relationship between d_m and d_{ae} measured

9

Formatted: Font: Italic
Formatted: Subscript
Formatted: Font: Italic
Formatted: Subscript
Formatted: Font: Italic
Formatted: Subscript
Formatted: Font: Italic
Formatted: Subscript

305 by a DMA and AAC, respectively. To simulate the transfer function of the DMA-AAC, the same particles

306 (d_m = 100 nm, m = 0.33 fg, D_{fm} = 2.28) as those used in the calculations of the DMA-CPMA were selected.

307 The corresponding d_{ae} was numerically solved using the known mass–mobility relationship. The transfer

308 function of the DMA-AAC selecting the same representative particles was calculated and is shown in

309 log(d_{ae})-log(d_m) (Fig. 4a). In the transfer function of DMA-CPMA, the classification regions of singly

310 charged particles and doubly charged particles are on the diagonal. The oblique line of particles population

311 is more likely to go through the region of doubly charged particles in the transfer function of DMA-

312 CPMA.Unlike the DMA-CPMA system, t The transfer functions of singly charged and doubly charged

313 particles are in parallel for the DMA-AAC, suggesting that the particles population is less likely to overlap

314 with the region of multiply charged particles. Using the example setups (d_m = 100 nm, Q_{DMA} = 0.3 L min^{-1},

315 β_{DMA} = 0.1, d_{ae} = 68.3 nm, Q_{AAC} = 0.3 L min^{-1}, β_{AAC} = 0.1.) of the DMA-AAC, truly monodispersed particles

316 are selected for spherical particles and typical soot particles.

317 Similar to the DMA-CPMA system, eliminating multiply charged particles requires that the $d_{ae,max}$ of the

318 AAC at $d_{m2,min}$ must be smaller than the d_{ae} of particles of interest, which can be derived from $d_{m2,min}$ and D_{fm}

319 (Eq. (27)),

320 $$d_{ae}\left(d_{m2,min}, D_{fm}\right) > d_{ae,max}\left(d_{m2,min}\right),$$

321 $$\Rightarrow D_{fm} > \frac{\log(2 \cdot \frac{1+\beta_{AAC}}{1+\beta_{DMA}})}{\log[\frac{2}{1+\beta_{DMA}} \cdot \frac{Cc(d_{m2,min})}{Cc(d_{m1})}]}, \tag{28}$$

322 This equation describes the minimum value of D_{fm} to eliminate the multiple charging effect. It is clearly

323 shown that the mobility resolution of the DMA and the relaxation time resolution of the AAC determine the

324 limiting condition, and the resolution of the AAC is more important compared with the resolution of the

325 DMA. The limiting condition is also related to the selected d_m of the DMA but independent of the selected

326 d_{ae} of the AAC (Fig. S1). Setting the same resolutions for the DMA and AAC, particle selection is more

327 susceptible to multiple charging effects when selecting small sizes. In Fig. 4a, the values of β_{DMA} and β_{AAC}

328 are 0.1, resulting in a minimum D_{fm} of 1.41.5 This D_{fm} is smaller than that for most aerosolswhich is the case

329 for most atmospheric aerosol particles. Hence, the selected particles of the DMA-AAC are truly

330 monodisperse regardless of the particle morphology. However, in actual operations, a larger sample flow rate

331 may be is required to satisfy the apparatus downstream, while the maximum sheath flow rate of the classifier

332 is restricted by the instrument design (e.g., 30 L min^{-1} for the DMA and 15 L min^{-1} for the AAC). In addition,

333 the maximum size ranges are also restricted by the sheath flow, so in some cases, a lower sheath flow rate is

334 required to select larger particles. When increasing β_{AAC} to 0.3 (decreasing the resolution of AAC) and

335 leaving β_{DMA} unchanged, the transfer function becomes broader (Fig. 4b). The minimum D_{fm} is 2.44, which

336 indicates that the multiple charging effect exists for typical soot particles with D_{fm} of 2.2-2.4. The line

337 representing soot particles overlaps with the region of doubly charged particles. Thus, reducing the

338 resolutions of the DMA or AAC is not suggested in actual operations.

339 We think the transfer functions of DMA-AAC or AAC-DMA are identical regardless of the order of DMA

340 and AAC. For example, we use AAC-DMA to select particles with d_{ae} of 68 nm and d_m of 100 nm. In Fig.

10

341 4a, the transfer function of AAC is the region between the horizontal lines of $d_{ae,max}$ (75 nm) and $d_{ae,min}$ (63

342 nm). The soot particles population (red line) goes through this region will be selected by AAC. The mobility

343 diameter distribution of these relaxation time selected particles is around 80 nm to 120 nm. Then the DMA

344 is fixed to select particles with d_m of 100 nm, the particles with double charges and the same mobility (d_m of

345 150 nm) have been excluded by AAC. As a result, AAC-DMA select monodispersed particles with d_{ae} of

346 68.3 nm and d_m of 100 nm. In Fig. 4b, the resolution of AAC is lower and transfer function of AAC is broader

347 than that in Fig. 4a. The soot particles population (red line) goes through the transfer function region between

348 the horizontal lines at d_{ae} of $d_{ae,max}$ (50 nm) and $d_{ae,min}$ (86 nm). The mobility diameter distribution of these

349 relaxation time selected particles is very wide from less than 80 nm to about 158 nm. Then these relaxation

350 time selected particles were charged and selected by DMA at d_m of 100 nm, singly charged particles with d_m

351 of 95 nm~106 nm and doubly charged particles with d_m of 142 nm~158 nm will be selected.

352 If we use the DMA-AAC, the particles are selected by DMA first. For example, in Fig. 4b, the transfer

353 function of DMA is shown as two vertical regions which particles with single and double charges can

354 penetrate. The soot particles (red line) goes through it and two populations of soot particles with mode d_m of

355 100 nm and 150 nm will be selected. The corresponding d_{ae} distributions of these singly and doubly charged

356 particles are 66 nm~70 nm and 81 nm~87 nm. These mobility-selected particles are selected at d_{ae} of 68.3

357 nm by AAC and the transfer function of AAC shows that particles with d_{ae} of 50 nm~86 nm can penetrate.

358 As a result, singly charged particles with d_{ae} of 66 nm ~70 nm and doubly charged particles with d_{ae} of 81

359 nm ~86 nm can be selected.

360 As a summary, the transfer functions of DMA-AAC and AAC-DMA in a static configuration are the same

361 no matter the ordering of DMA and AAC.

362 **3.2 Evaluation of the multiple charging effect**

363 To quantify the possible biases of the multiple charging effect in the DMA-CPMA system, we conducted a

364 soot experiment, as demonstrated in Fig. 1. For each mobility-selected particles, the distributions of number

365 density as a function of d_{ae} and m were determined by the scans. These distributions were then fit to a log-

366 normal to determine the modal values of ($d_{ae,c}$, and m_c) and from these values the ρ_{eff} were determined. the

367 corresponding d_{ae} and m were determined using the AAC and CPMA scan modes, from which the effective

368 densities were derived. The uncertainties of $d_{ae,c}$ and m_c were standard deviation of multiple measurements.

369 Representative plots for the measured spectral density distributions of mass and aerodynamic diameter d_{ae} of

370 particles with d_m of 150 nm and 250 nm are shown in Fig. S2. The results are summarized in Table 2. The

371 fitted values of D_{fm} and k_f were 2.28 and 7.49×10^{-6} fg, respectively, indicating a fractal structure, which is

372 the same as in previous studies (Pei et al., 2018). The effective densities of generated soot particles vary

373 from >500 kg m^{-3} at d_m = 80 nm to <300 kg m^{-3} at d_m of 250 nm for the two methods determined by DMA-

374 CPMA and DMA-AAC. In general, the deviation of values of ρ_{eff} measured by DMA-CPMA and DMA-

375 AAC monotonically decreases with increasing particle size. The deviation is 7.65% for particles of 80 nm,

11

376 whereas it decreased to <1% for particles larger than 200 nm. The results reveal a strict agreement between

377 the two methods for retrieving the particle effective density.

378 According to Fig. 3, the critical slopes of PP_0 for soot particles with d_m of 80 nm, 100 nm, 150 nm, 200 nm

379 and 250 nm are 2.46, 2.41, 2.29, 2.17 and 2.08, respectively. The measured D_{fm} of 2.28 is smaller than the

380 calculated PP_0 for particles with d_m smaller than 200 nm, which suggests that the contributions from the

381 multiply charged particles cannot be eliminated.

382 When selecting particles with d_m of 80 nm and m of 0.16 fg, the corresponding DMA-CPMA transfer function

383 is shown in Fig. 5a. DMA-CPMA is set to select singly charged particles with d_m of 80 nm and m of 0.16 fg,

384 while the doubly charged particles with d_m of 119.3 nm and m of 0.32 fg will also be selected and the transfer

385 function is presented as upper right region. Soot particles curve (red line) goes through the upper-right region

386 which doubly charged particle can penetrate (d_m of 113 nm~118 nm, m of 0.35 fg~0.39 fg). As a result, we

387 conclude that multiple charging effect still exists when DMA-CPMA select soot particles with d_m of 80 nm

388 and m of 0.16 fg The particle population overlaps the transfer function region of doubly charged particles,

389 suggesting the potential interferences of doubly charged particles in DMA-CPMA selection. Since the

390 classification of the AAC is different from the DMA and CPMA, the aerodynamic size distributions of

391 mobility- and mass- selected particles were characterized. Fig. 5b shows the particles number density

392 aerodynamic size distribution ($PNSD_{ae}$) scanned by the AAC. For each measurement, $PNSD_{ae}$ was fitted

393 using log-normal distributions, and three peaks corresponding to singly, doubly and triply charged particles

394 were identified. The fractional number concentrations (f_N) of particles with different charging state is

395 expressed as follows,

396 $$f_{N,n} = \frac{\int_{d_{ae,low min}}^{d_{ae,high max}} \frac{dN_n}{d\log(d_{ae})} d\log(d_{ae})}{\sum_{n=1}^{3} \int_{d_{ae,low min}}^{d_{ae,high max}} \frac{dN_n}{d\log(d_{ae})} d\log(d_{ae})}.$$

397 (29)

398 where $f_{N,n}$ and N_n are the fractional number concentration and number concentration of particles bearing n

399 charges. N_n stands for the number concentration of particles with n charges. $d_{ae,low min}$ and $d_{ae,high max}$ denote the

400 minimum and maximum values of d_{ae} scanned by AAC, respectively. The uncertainties are standard

401 deviations of multiple measurements. Some small particles remaining in the AAC induced the peak at d_{ae}

402 <40 nm. These residual particles were measured even if the sample flow was filtered. For particles with d_m

403 = 80 nm, The mean modal d_{ae} values were 53.9 nm, 60.6 nm and 70.9 nm, and the corresponding d_{ae} values

404 were calculated as 51.5 nm, 62.0 nm and 70.7 nm using Eq. (1) and Eq. (16 17). The experimental results are

405 consistent with the theoretical results with deviations within 5.3%.

406 In contrast, w When selecting particles with d_m of 200 nm and m of 1.28 fg, the transfer function is shown in

407 Fig. 6a. The PP_0 slope of 2.17 is smaller than that D_{fm} of 2.28, and the generated particles population does

408 not overlap with the block of doubly charged particles; thus, the DMA-CPMA classified particles were truly

409 monodispersed. $PNSD_{ae}$ measured by the AAC is unimodal, implying that the classified particles were singly

410 charged (Fig. 6b).

411 The results of other experiments are shown in Fig. S3. Although the critical slope of PP_0 when selecting 150

412 nm particles is close to D_{fm} and the transfer function of DMA-CPMA also showed that negligible multiply

413 charged particles would be selected (Fig. S3d), doubly charged particles were measured in $PNSD_{ae}$ (Fig. S3e).

414 These doubly charged particles were selected, probably owing to particle diffusion. The nondiffusion models

415 were used to calculate the transfer function, but the transfer function can be broader because of diffusion. In

416 summary, for a type of particle with the same mass–mobility relationship, the possibility of multiple charging

417 increases for small particles when selected by the DMA-CPMA system, which is consistent with the

418 theoretical calculation in Sect. 3.1.

419 **3.3 Atmospheric implication**

420 The DMA-APM and DMA-CPMA systems are usually adopted to eliminate multiply charged particles in

421 soot aerosol studies. Although they might fail to select monodispersed particles, downstream measurements

422 by instruments such as a single-particle soot photometer (SP2) will not be interfered with, which characterizes

423 the distinct information of a single particle. Nevertheless, for techniques measuring the properties of an entire

424 aerosol population, e.g., scattering coefficient by a nephelometer or absorption coefficient by a photoacoustic

425 spectrometer, multiply charged particles can induce significant bias. A previous study (Radney and

426 Zangmeister, 2016) noted that the DMA-APM failed to resolve multiply charged particles for soot particles

427 when selecting 150 nm flame-generated particles, which caused a 110% error in extinction measurement. To

428 investigate the multiple charging effect for DMA-CPMA classification, the optical absorption coefficient of

429 particles with different charging states after DMA-CPMA classification was calculated from $PNSD_{ae}$. Mie

430 theory was used to calculate the theoretical absorption coefficient at a wavelength of 550 nm. Mie theory is

431 probably not the "best" method to use here since soot particles are aspherical agglomerates. Realistically,

432 however, the Mie comparison is only being used to prove a point about the impact of multiple charging.

433 Therefore, in this instance, any errors in the calculated optical properties are somewhat inconsequential. The

434 refractive index used in the Mie code was 1.95+0.79i (Bond and Bergstrom, 2006). The $PNSD_{ae}$ for different

435 charging state particles was converted to volume-equivalent diameter size distributions ($PNSD_{ve}$), which was

436 used in Mie theory to determine the absorption coefficient. The method to calculate $PNSD_{ve}$ is described in

437 Sect. S1. Subsequently, the absorption coefficient, α_{abs}, was derived using Mie theory and the $PNSD_{ve}$ of

438 particles with different charging states. The fractional absorption coefficient (f_{abs}) for particles with different

439 charging state was calculated using Eq. (28) by replacing N with α_{abs} and replacing d_{ve} with d_{ve} as follows,

440 $$f_{abs,n} = \frac{\int_{d_{ve,low,n}}^{d_{ve,high,n}} \frac{d\alpha_{abs,n}}{d\log(d_{ve})} d\log(d_{ve})}{\sum_{i=1}^{3} \int_{d_{ve,low,n}}^{d_{ve,high,n}} \frac{dN_n}{d\log(d_{ve})} d\log(d_{ve})} , \tag{30}$$

441 where $f_{abs,n}$ and $\alpha_{abs,n}$ are the fractional absorption coefficient and absorption coefficient of particles bearing

442 n charges, respectively. $d_{ve,low,n}$ and $d_{ve,high,n}$ denote the minimum and maximum value of d_{ve} of particles with

443 n charges, which are converted from $d_{ae,low}$ and $d_{ae,high}$ scanned by AAC, respectively.

444 The overestimation of mass absorption cross-section (MAC) was calculated by

13

445
$$\frac{\Delta \mathrm{MAC}}{\mathrm{MAC}} = \frac{\frac{\alpha_{\mathrm{abs,tot}}}{m_{\mathrm{p}} N_{\mathrm{tot}}} - \frac{f_{\mathrm{abs,1}} \cdot \alpha_{\mathrm{abs,tot}}}{m_{\mathrm{p}} \cdot f_{\mathrm{N,1}} \cdot N_{\mathrm{tot}}}}{\frac{f_{\mathrm{abs,1}} \cdot \alpha_{\mathrm{abs,tot}}}{m_{\mathrm{p}} \cdot f_{\mathrm{N,1}} \cdot N_{\mathrm{tot}}}} = \frac{f_{\mathrm{N,1}}}{f_{\mathrm{abs,1}}} - 1 \ . \tag{31}$$

446 where $\alpha_{\mathrm{abs,tot}}$ and N_{tot} is the total absorption coefficient and number concentration of particles selected by
447 DMA-CPMA, respectively. m_{p} is the actual mass of singly charged particles selected by DMA-CPMA. The
448 uncertainties were calculated from propagation of errors. For soot particles with diameters <200 nm, the
449 optical absorption contributions of particles with different charging states and the ~~mass absorption cross~~
450 ~~section~~ (MAC) overestimation are summarized in Table 3. For soot particles with a diameter of 80 nm, the
451 contributions of particles with different charging states are shown in Fig. 5c. Doubly charged particles only
452 account for 26.7% ±3.0% of the total number concentration but provide a large fractional contribution to the
453 total absorption (45.7% ±4.2%). Additionally, a small fraction (1.1% ±0.4%) of triply charged particles
454 accounted for 3.7% ±1.5% of the absorption. As a result, the MAC was overestimated by ~~43.0~~42.7% ±~~2.7~~9.1%,
455 and the directive radiative force (DRF) was overestimated by ~~43.0~~42.7% ±~~2.7~~9.1%. The DRF was calculated
456 using previous global climate models (Bond et al., 2016). For particles selected by the DMA-CPMA at a d_{m}
457 of 200 nm and an m of 1.28 fg, the selected particles were truly dispersed, and the measured optical properties
458 were valid (Fig. 6c).
459 A large amount of 70 nm -90 nm soot particles was emitted from diesel engine (Wierzbicka et al., 2014), and
460 neglecting the multiple charging effect in the measurement of mass-specific MAC on this size range will
461 result in significant bias in the estimation of radiative forcing of automobile-emitted soot particles, which
462 may lead to large errors in climate model.
463 According to Table 3, the number fraction of doubly charged particles declines with the size of the nominated
464 particles, i.e., 26.7% ±3.0% and 17.6% ±0.5% for 80 and 100 nm particles, respectively, but only 4.2% ±1.1%
465 for 150 nm particles. Accordingly, the MAC was largely overestimated for 80 and 100 nm particles
466 (~~43.0~~42.7% ±~~2.7~~9.1% and ~~27.9~~28.0% ±~~0.8~~1.8%, respectively) but moderately overestimated for 150 nm
467 particles (~~9.3~~9.2% ±~~2.6~~4.1%). To summarize, our results indicated that the combination of tandem classifiers
468 is not sufficient to completely eliminate multiply charged particles when selecting small flame-generated
469 soot particles, which introduced noticeable bias for absorption measurements and led to overestimation of
470 the MAC. As a result, the DRF of soot particles was also overestimated.

471 **4 Conclusion**

472 In this study, we demonstrate the transfer functions of DMA-CPMA and DMA-AAC and discuss their
473 limitations to eliminate multiply charged particles. For aspherical particles, there is no guarantee that the
474 multiple charging effect can be avoided in DMA-CPMA or DMA-AAC systems. Usually, a DMA-AAC can
475 select truly monodisperse particles, but the method can suffer from multiple charging when decreasing the
476 resolutions of the DMA and AAC. The ability of the DMA-CPMA to eliminate multiple charging effect
477 mainly depends on the particle morphology and the instrument resolutions. ~~Under the same setups of DMA-~~
478 ~~CPMA, t~~This tandem system is more sensitive to multiple charging effect with decreasing D_{fm} and decreasing

14

479 nominal size of particles. The DMA-CPMA failed to eliminate multiply charged particles when selecting
480 soot particles with diameters < 150 nm. Although doubly charged particles accounted for a small fraction of
481 the number concentration, they contributed most significantly to light absorption, which indicated that
482 multiply charged particles can induce an obvious contribution to light absorption and lead to an
483 overestimation of DRF for flame-generated soot particles.

484

485 *Code/Data availability*. Code/Data are available upon request.
486 *Author contributions*. ZW determined the main goal of this study. YS and XP designed the methods. YS
487 carried them out and prepared the paper with contributions from all coauthors. YS, HL and JZ analyzed the
488 optical data.
489 *Competing interests*. The authors declare that they have no conflicts of interest.

Appendix A

Table A1. Nomenclature~~Symbols used in this study~~

Parameter~~μ~~	Definition~~Air viscosity~~
~~β~~	~~The ratio of flow rates of aerosol flow and sheath flow, Q_a/Q_{sh}~~
~~τ~~	~~Relaxation time~~
~~ω_1~~	~~Rotational speed of the inner electrode~~
~~ω_2~~	~~Rotational speed of the outer electrode~~
~~$\hat{\omega}$~~	~~ω_1/ω_2~~
~~δ~~	~~Half width of the gap between the two electrodes~~
~~Ω~~	~~Transfer function~~
~~ρ_0~~	~~Standard density, which equals 1 kg/m³~~
~~τ~~	~~Relaxation time~~
~~τ^*~~	~~τ at the maximum of the transfer function~~
~~$\tilde{\tau}$~~	~~Dimensionless particle relaxation time, $\tilde{\tau} = \tau/\tau^*$~~
~~ρ_{eff}~~	~~Effective density~~
~~k_f~~	~~Mass-mobility pre-exponential factor~~
~~α_{abs}~~	~~Absorption coefficient~~
B	Mechanical mobility
$C_c(d_p)$	Cunningham slip correction factor
c_r	Particle migration velocity

Symbol	Definition
D_{fm}	Mass-mobility exponent
d_{ae}	Aerodynamic equivalent diameter
$d_{ae,c}$	the geometric mean of d_{ae} distribution measured by AAC-CPC
$d_{ae,high}$	The maximum value of d_{ae} scanned by AAC
$d_{ae,low}$	The minimum value of d_{ae} scanned by AAC
$d_{ae,max}$	The maximum d_{ae} of particles that can be selected in AAC classification
$d_{ae,min}$	The minimum d_{ae} of particles that can be selected in AAC classification
d_m	Mobility equivalent diameter
$d_{mn,max}$	The maximum d_m of particles with n charges that can be selected in DMA classification
$d_{mn,min}$	The minimum d_m of particles with n charges that can be selected in DMA classification
d_{ve}	Volume-equivalence size
D_{fm}	Mass-mobility exponent
e	Elementary charge
$f_{N,n}$	The fractional number concentration of particles with n charges
$f_{abs,n}$	The fractional absorption coefficient of particles with n charges
k_f	Mass-mobility pre-exponential factor
L	Length of DMA, CPMA or AAC
m	Particle mass
m_c	the geometric mean of m distribution measured by CPMA-CPC
$m_{n,max}$	The maximum m of particles with n charges that can be selected in CPMA classification
$m_{n,min}$	The minimum m of particles with n charges that can be selected in CPMA classification
n	Number of elementary charges on the particle
N_{tot}	The total number concentration of particles selected by DMA-CPMA
PNSD	Particle number size distribution
$PNSD_{ae}$	Particle number aerodynamic size distribution
$PNSD_{ve}$	Particle number volume-equivalent size distribution
q	Electrical charge on the particle
Q_a	Sample flow rate
Q_{sh}	Sheath flow rate
q	Electrical charge on the particle
R_m	Mass resolution of CPMA
r_a	Lower initial radial position that passes through the classifier
r_b	Upper initial radial position that passes through the classifier

r_1	Inner radium
r_2	Outer radium
$\hat{r}$	r_1/r_2
R_m	Mass resolution of CPMA
t	Time
~~V~~	~~Voltage between the two electrodes of DMA or CPMA~~
$\bar{v}$	Average flow velocity
v_z	Axial flow distribution
v_θ	Velocity profile in the angular direction
V	Voltage between the two electrodes of DMA or CPMA
Z_p	Electrical mobility
$Z_p^* \cancel{Z_\mathrm{p}^*}$	Z_p at the maximum transfer function of DMA
~~Z_p~~	~~Electrical mobility~~
$\tilde{Z}_p$	$Z_p/Z_p^* \cancel{Z_\mathrm{p}^*}$
α ~~β~~	Azimuthal flow velocity distribution parameter
α_abs	Absorption coefficient
$\alpha_\mathrm{abs,tot}$	The total absorption coefficient of particles selected by DMA-CPMA
~~β~~	~~Azimuthal flow velocity distribution parameter~~
β_AAC	The ratio of flow rates of aerosol flow and sheath flow of AAC
β_DMA	The ratio of flow rates of aerosol flow and sheath flow of DMA
δ	Half width of the gap between the two electrodes
μ	Air viscosity
ρ_0	Standard density, which equals 1 kg/m³
ρ_eff	Effective density
σ_m	The geometric standard deviation of m distribution
σ_ae	The geometric standard deviation of d_ae distribution
τ	Relaxation time
τ^*	τ at the maximum of the transfer function
$\tilde{\tau}$	Dimensionless particle relaxation time, $\tilde{\tau} = \tau/\tau^*$
ω_1	Rotational speed of the inner electrode
ω_2	Rotational speed of the outer electrode
$\hat{\omega}$	ω_1/ω_2
Ω	Transfer function

Formatted Table

Formatted Table

Formatted Table

495 **References**

496 Ait Ali Yahia, L., Gehin, E., and Sagot, B.: Application of the The Rmophoretic Annular Precipitator (TRAP)

497 for the study of soot aggregates morphological influence on their thermophoretic behaviour, J. Aerosol Sci.,

498 113, 40-51, https://doi.org/10.1016/j.jaerosci.2017.07.018, 2017.

499 Biskos, G., Malinowski, A., Russell, L. M., Buseck, P. R., and Martin, S. T.: Nanosize Effect on the

500 Deliquescence and the Efflorescence of Sodium Chloride Particles, Aerosol Sci. Technol., 40, 97-106,

501 https://doi.org/10.1080/02786820500484396, 2006.

502 Bond, T. C., and Bergstrom, R. W.: Light Absorption by Carbonaceous Particles: An Investigative Review,

503 Aerosol Sci. Technol, 40, 27-67, https://doi.org/10.1080/02786820500421521, 2006.

504 Bond, T. C., Doherty, S. J., Fahey, D. W., Forster, P. M., Berntsen, T., DeAngelo, B. J., Flanner, M. G., Ghan,

505 S., Kärcher, B., Koch, D., Kinne, S., Kondo, Y., Quinn, P. K., Sarofim, M. C., Schultz, M. G., Schulz, M.,

506 Venkataraman, C., Zhang, H., Zhang, S., Bellouin, N., Guttikunda, S. K., Hopke, P. K., Jacobson, M. Z.,

507 Kaiser, J. W., Klimont, Z., Lohmann, U., Schwarz, J. P., Shindell, D., Storelvmo, T., Warren, S. G., and

508 Zender, C. S.: Bounding the role of black carbon in the climate system: A scientific assessment, J. Geophys.

509 Res.: Atmos.: Atmospheres, 118, 5380-5552, https://doi.org/10.1002/jgrd.50171, 2013.

510 Cheng, Y., Su, H., Koop, T., Mikhailov, E., and Pöschl, U.: Size dependence of phase transitions in aerosol

511 nanoparticles, Nat. Commun., 6, https://doi.org/10.1038/ncomms6923, 2015.

512 Dastanpour, R., Momenimovahed, A., Thomson, K., Olfert, J., and Rogak, S.: Variation of the optical

513 properties of soot as a function of particle mass, Carbon, 124, 201-211,

514 https://doi.org/10.1016/j.carbon.2017.07.005, 2017.

515 Dusek, U., Frank, G. P., Hildebrandt, L., Curtius, J., Schneider, J., Walter, S., Chand, D., Drewnick, F., Hings,

516 S., Jung, D., Borrmann, S., and Andreae, M. O.: Size Matters More Than Chemistry for Cloud-Nucleating

517 Ability of Aerosol Particles, Science, 312, 1375-1378, https://doi.org/10.1126/science.1125261, 2006.

518 Ehara, K., Hagwood, C., and Coakley, K. J.: Novel method to classify aerosol particles according to their

519 mass-to-charge ratio—Aerosol particle mass analyser, J. Aerosol Sci, 27, 217-234,

520 https://doi.org/10.1016/0021-8502(95)00562-5, 1996.

521 ~~Johnson, T. J., Nishida, R., Irwin, M., Symonds, J. P.R., Olfert, J. S., Boies, A.: Agreement Between Different~~

522 ~~Aerosol Classifiers Using Spherical Particles, https://doi.org/10.13140/RG.2.2.30999.27043, 2018.~~

523 Johnson, T. J.; Nishida, R. T.; Zhang, X.; Symonds, J. P. R.; Olfert, J. S.; Boies, A. M., Generating an aerosol

524 of homogeneous, non-spherical particles and measuring their bipolar charge distribution. J. Aerosol Sci, 153.

525 https://doi.org/10.1016/j.jaerosci.2020.105705, 2021.

526 Johnson, T. J.; Olfert, J. S.; Cabot, R.; Treacy, C.; Yurteri, C. U.; Dickens, C.; McAughey, J.; Symonds, J. P.

527 R., Steady-state measurement of the effective particle density of cigarette smoke. J. Aerosol Sci, 75, 9-16,

528 https://doi.org/10.1016/j.jaerosci.2014.04.006, 2014.

529 Kazemimanesh, M., Dastanpour, R., Baldelli, A., Moallemi, A., Thomson, K. A., Jefferson, M. A., Johnson,

530 M. R., Rogak, S. N., and Olfert, J. S.: Size, effective density, morphology, and nano-structure of soot particles

18

531 generated from buoyant turbulent diffusion flames, J. Aerosol Sci., 132, 22-31,
532 https://doi.org/10.1016/j.jaerosci.2019.03.005, 2019a.

533 Kazemimanesh, M., Moallemi, A., Thomson, K., Smallwood, G., Lobo, P. and Olfert, J.S.: A novel miniature
534 inverted-flame burner for the generation of soot nanoparticles. Aerosol Sci. and Technol., 53(2), 184-195,
535 https://doi.org/10.1080/02786826.2018.1556774, 2019b.

536 Kazemimanesh, M., Rahman, M.M., Duca, D., Johnson, T.J., Addad, A., Giannopoulos, G., Focsa, C. and
537 Boies, A.M.: A comparative study on effective density, shape factor, and volatile mixing of non-spherical
538 particles using tandem aerodynamic diameter, mobility diameter, and mass measurements. J. Aerosol Sci.,
539 161, 105930, https://doi.org/10.1016/j.jaerosci.2021.105930, 2022.

540 Knutson, E. O., and Whitby, K. T.: Aerosol classification by electric mobility: apparatus, theory, and
541 applications, J. Aerosol Sci., 6, 443-451, https://doi.org/10.1016/0021-8502(75)90060-9, 1975.

542 Kuwata, M.: Particle Classification by the Tandem Differential Mobility Analyzer–Particle Mass Analyzer
543 System, Aerosol Sci. Technol., 49, 508-520, https://doi.org/10.1080/02786826.2015.1045058, 2015.

544 Moallemi, A.; Kazemimanesh, M.; Corbin, J. C.; Thomson, K.; Smallwood, G.; Olfert, J. S.; Lobo, P.,
545 Characterization of black carbon particles generated by a propane-fueled miniature inverted soot generator.
546 J. Aerosol Sci., 135, 46-57, https://doi.org/10.1016/j.jaerosci.2019.05.004, 2019.

547 Olfert, J. S., and Collings, N.: New method for particle mass classification—the Couette centrifugal particle
548 mass analyzer, J. Aerosol Sci., 36, 1338-1352, https://doi.org/10.1016/j.jaerosci.2005.03.006, 2005.

549 Park, K., Cao, F., Kittelson, D. B, and Mcmurry, P. H.: Relationship between Particle Mass and Mobility for
550 Diesel Exhaust Particles, Environ. Sci. & Technol., 37, 577-583, https://doi.org/10.1021/es025960v, 2003.

551 Park, K., Dutcher, D., Emery, M., Pagels, J., Sakurai, H., Scheckman, J., Qian, S., Stolzenburg, M. R., Wang,
552 X., Yang J., and McMurry P. H.: Tandem Measurements of Aerosol Properties—A Review of Mobility
553 Techniques with Extensions. Aerosol Sci. and Techno., 42, 801-816,
554 https://doi.org/10.1080/02786820802339561, 2008.

555 Pei, X., Hallquist, M., Eriksson, A. C., Pagels, J., Donahue, N. M., Mentel, T., Svenningsson, B., Brune, W.,
556 and Pathak, R. K.: Morphological transformation of soot: investigation of microphysical processes during
557 the condensation of sulfuric acid and limonene ozonolysis product vapors, Atmos. Chem. Phys., 18, 9845-
558 9860, https://doi.org/10.5194/acp-18-9845-2018, 2018.

559 Radney, J. G., Ma, X., Gillis, K. A., Zachariah, M. R., Hodges, J. T., and Zangmeister, C. D.: Direct
560 Measurements of Mass-Specific Optical Cross Sections of Single-Component Aerosol Mixtures, Anal.
561 Chem., 85, 8319-8325, https://doi.org/10.1021/ac401645y, 2013.

562 Radney, J. G., and Zangmeister, C. D.: Practical limitations of aerosol separation by a tandem differential
563 mobility analyzer–aerosol particle mass analyzer, Aerosol Sci. Technol., 50, 160-172,
564 https://doi.org/10.1080/02786826.2015.1136733, 2016.

565 Rissler, J., Messing, M. E., Malik, A. I., Nilsson, P. T., Nordin, E. Z., Bohgard, M., Sanati, M., and Pagels,
566 J. H.: Effective Density Characterization of Soot Agglomerates from Various Sources and Comparison to
567 Aggregation Theory, Aerosol Sci. Technol., 47, 792-805, 10.1080/02786826.2013.791381, 2013.

19

568 Shiraiwa, M., Kondo, Y., Iwamoto, T., and Kita, K.: Amplification of Light Absorption of Black Carbon by
569 Organic Coating, Aerosol Sci. & Technol., 44, 46-54, https://doi.org/10.1080/02786820903357686, 2010.
570 Sipkens, T. A., Olfert, J. S., and Rogak, S. N.: New approaches to calculate the transfer function of particle
571 mass analyzers, Aerosol Sci. Technol., 54, 111-127, https://doi.org/10.1080/02786826.2019.1680794, 2019.
572 Stolzenburg, M. R., and McMurry, P. H.: Equations Governing Single and Tandem DMA Configurations
573 and a New Lognormal Approximation to the Transfer Function, Aerosol Sci. Technol., 42, 421-432,
574 https://doi.org/10.1080/02786820802157823, 2008.
575 Swietlicki, E., Hansson, H. C., Hämeri, K., Svenningsson, B., Massling, A., McFiggans, G., McMurry, P. H.,
576 Petäjä T., Tunved, P., Gysel, M., Topping, D., Weingartner, E., Baltensperger, U., Rissler, J., Wiedensohler,
577 A., and Kulmala, M.: Hygroscopic properties of submicrometer atmospheric aerosol particles measured with
578 H-TDMA instruments in various environments – a review, Tellus B, 60, 432–469,
579 https://doi.org/10.1111/j.1600-0889.2008.00350.x, 2008.
580 Tavakoli, F., and Olfert, J. S.: An Instrument for the Classification of Aerosols by Particle Relaxation Time:
581 Theoretical Models of the Aerodynamic Aerosol Classifier, Aerosol Sci. Technol., 47, 916-926,
582 https://doi.org/10.1080/02786826.2013.802761, 2013.
583 Tavakoli, F., and Olfert, J. S.: Determination of particle mass, effective density, mass–mobility exponent,
584 and dynamic shape factor using an aerodynamic aerosol classifier and a differential mobility analyzer in
585 tandem, J. Aerosol Sci., 75, 35-42, https://doi.org/10.1016/j.jaerosci.2014.04.010, 2014.
586 Wiedensohler, A., Birmili, W., Nowak, A., Sonntag, A., Weinhold, K., Merkel, M., Wehner, B., Tuch, T.,
587 Pfeifer, S., Fiebig, M., Fjäraa, A. M., Asmi, E., Sellegri, K., Depuy, R., Venzac, H., Villani, P., Laj, P., Aalto,
588 P., Ogren, J. A., Swietlicki, E., Williams, P., Roldin, P., Quincey, P., Hüglin, C., Fierz-Schmidhauser, R.,
589 Gysel, M., Weingartner, E., Riccobono, F., Santos, S., Grüning, C., Faloon, K., Beddows, D., Harrison, R.,
590 Monahan, C., Jennings, S. G., O'Dowd, C. D., Marinoni, A., Horn, H.-G., Keck, L., Jiang, J., Scheckman, J.,
591 McMurry, P. H., Deng, Z., Zhao, C. S., Moerman, M., Henzing, B., de Leeuw, G., Löschau, G., and Bastian,
592 S.: Mobility particle size spectrometers: harmonization of technical standards and data structure to facilitate
593 high quality long-term observations of atmospheric particle number size distributions, Atmos. Meas. Tech.,
594 5, 657–685, https://doi.org/10.5194/amt-5-657-2012, 2012.
595 Yao, Q., Asa-Awuku, A., Zangmeister, C. D., and Radney, J. G.: Comparison of three essential sub-
596 micrometer aerosol measurements: Mass, size and shape, Aerosol Sci. Technol., 1-18,
597 https://doi.org/10.1080/02786826.2020.1763248, 2020.
598 Zangmeister, C. D., You, R., Lunny, E. M., Jacobson, A. E., Okumura, M., Zachariah, M. R., and Radney, J.
599 G.: Measured in-situ mass absorption spectra for nine forms of highly-absorbing carbonaceous aerosol,
600 Carbon, 136, 85-93, https://doi.org/10.1016/j.carbon.2018.04.057, 2018.
601 Zhang, R., Khalizov, A. F., Pagels, J., Zhang, D., Xue, H., and McMurry, P. H.: Variability in morphology,
602 hygroscopicity, and optical properties of soot aerosols during atmospheric processing, Proc. Natl. Acad. Sci.,
603 105, 10291, https://doi.org/10.1073/pnas.0804860105, 2008.
604

605

Table 1 Dimensions of the three classifiers used for transfer function calculation

Parameter	DMA	CPMA	AAC
r_1 (mm)	9.37	100	43
r_2 (mm)	19.61	103	45
L (mm)	44.369	200	210
ω_2/ω_1	—	0.945	—

606

607
608 **Table 2. Mobility diameter, mass, aerodynamic diameter, effective densities calculated by DMA-AAC and DMA-CPMA, and the deviation between them for fresh soot particles in the size range of 80–250 nm.**

d_m (nm)	~~M~~m_c (fg)	$d_{ae,c}$ (nm)	$\rho_{DMA\text{-}AAC}$ (kg m^{-3})	$\rho_{DMA\text{-}CPMA}$ (kg m^{-3})	Deviation
80	0.16±0.01	48.2±0.3	551.2±6.9	596.8±37.30	7.65%
100	0.27±0.01	54.8±0.3	488.0±5.32	515.7±19.10	5.38%
150	0.66±0.07	67.8±0.3	359. 1±3.22	373.5±39.61	3.86%
200	1.28±0.10	82.1±0.6	303.2±4.44	305.6±23.87	0.77%
250	2.17±0.16	95.9±0.9	262.8±4.92	265.2±19.56	0.90%

Formatted: Subscript

609

610
611 **Table 3. Number concentration fractions and absorption contributions for different size fresh soot particles with single, double or triple charges and the overestimation of MAC accordingly.**

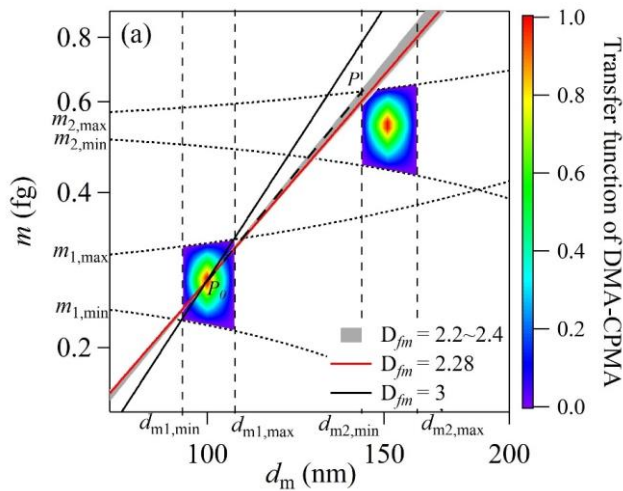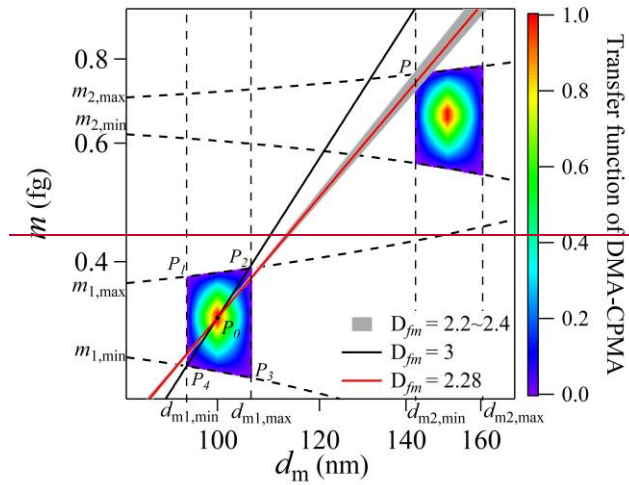| d_m (nm)	$f_{N,1}$(%)	$f_{abs,1}$(%)	$f_{N,2}$(%)	$f_{abs,2}$(%)	$f_{N,3}$(%)	$f_{abs,3}$(%)	MAC overestimation(%)
80	72.2±2.5	50.6±2.7	26.7±3.0	45.7±4.2	1.1±0.4	3.7±1.5	~~43.0~~2.7±~~2.7~~9.1
100	82.4±0.5	64.4±0.8	17.6±0.5	35.6±0.8	-	-	~~27.9~~8.0±~~0~~1.8
150	95.8±1.2	87.7±3.1	4.2±1.1	12.3±3.1	-	-	9.~~3~~2±~~2.6~~4.1

Formatted Table

612
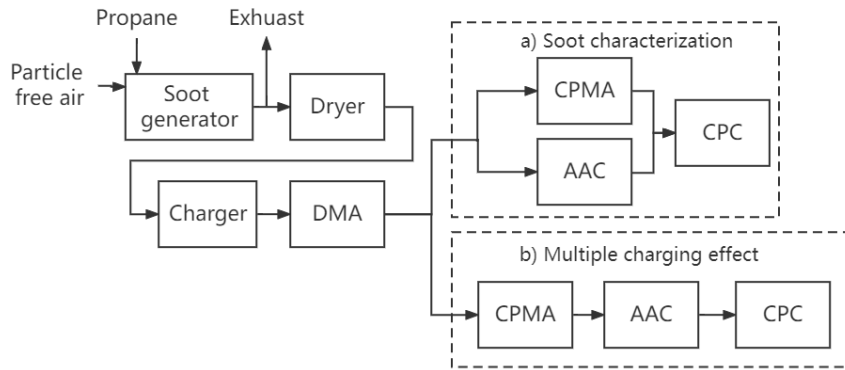
613
614 **Figure 1: Schematic of the experimental setup: (a) soot characterization and (b) evaluation of multiple charging**
615 **effects.**

Figure 2: Example of the DMA-CPMA transfer function of flame-generated soot particles (Pei et al., 2018) in $\log(m)$-$\log(d_m)$. The following parameter set was employed for the calculations: $d_m = 100$ nm, $\beta_{DMA} = 0.1$, $m = 0.33$ fg, Q_{CPMA}=0.3 L min^{-1}, $R_m = 8$. The color blocks are the transfer function of DMA-CPMA, with the rainbow color representing the transfer function for singly charged (lower left block) and doubly charged (upper right block) particles. The black and red solid lines are particles populations with D_{fm} values of 3 and 2.28, respectively. The gray region is the particle population with D_{fm} of 2.2-2.4, which is typical for soot aerosols. The dashed dotted lines are the limits of d_m and m of DMA and CPMA, respectively. The dashed line is the critical slope of PP_0. The DMA–CPMA transfer function for +2 particles does not overlap with the line for spherical particles with a single charge (D_{fm}=3).

627

628
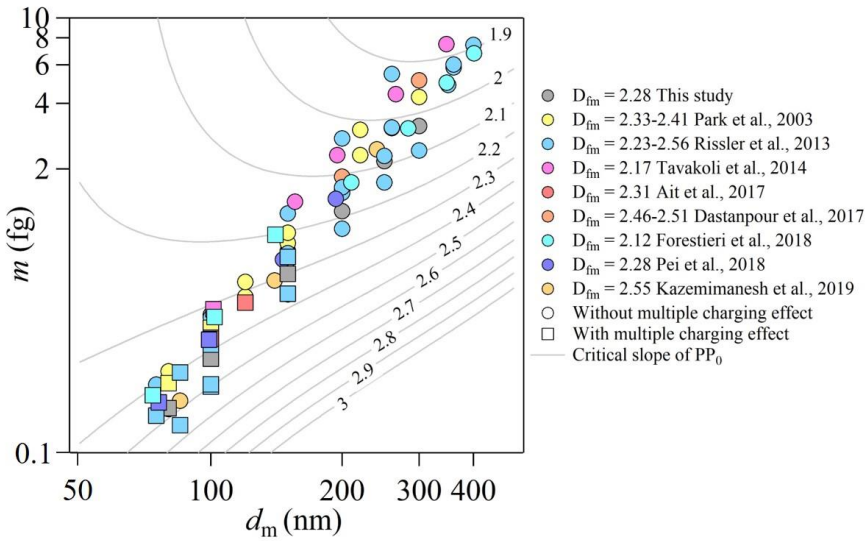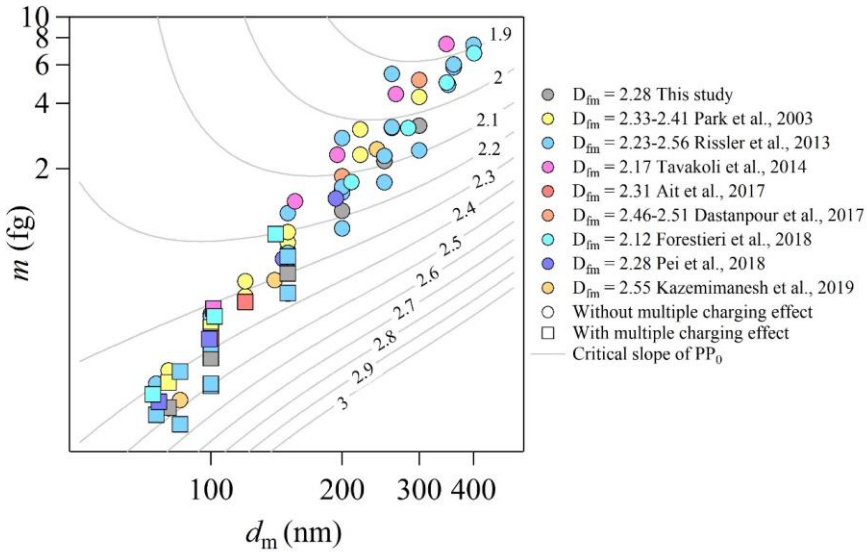
Figure 3: Variations of the slope of PP$_0$ as a function of classified d_m and m. The following parameter set was employed for the calculations: β_{DMA} = 0.1, Q_{CPMA}=0.3 L min^{-1}, R_m = 8. The contour lines denote the <u>critical</u> slope of PP$_0$, with values labeled on them. The data points are soot particles measured in the literature (Park et al., 2003; Rissler et al., 2013; Tavakoli et al., 2014; Ait Ali Yahia et al., 2017; Dastanpour et al., 2017; Forestieri et al., 2018; Pei et al., 2018; Kazemimanesh et al., 2019) and generated in this study (see details in Sect 3.2). The D_{fm} values of these data points are listed in the legend. The data points become square when D_{fm} is smaller than the critical slope of PP0 in the background, i.e., the potential multiple charging effect may exist.
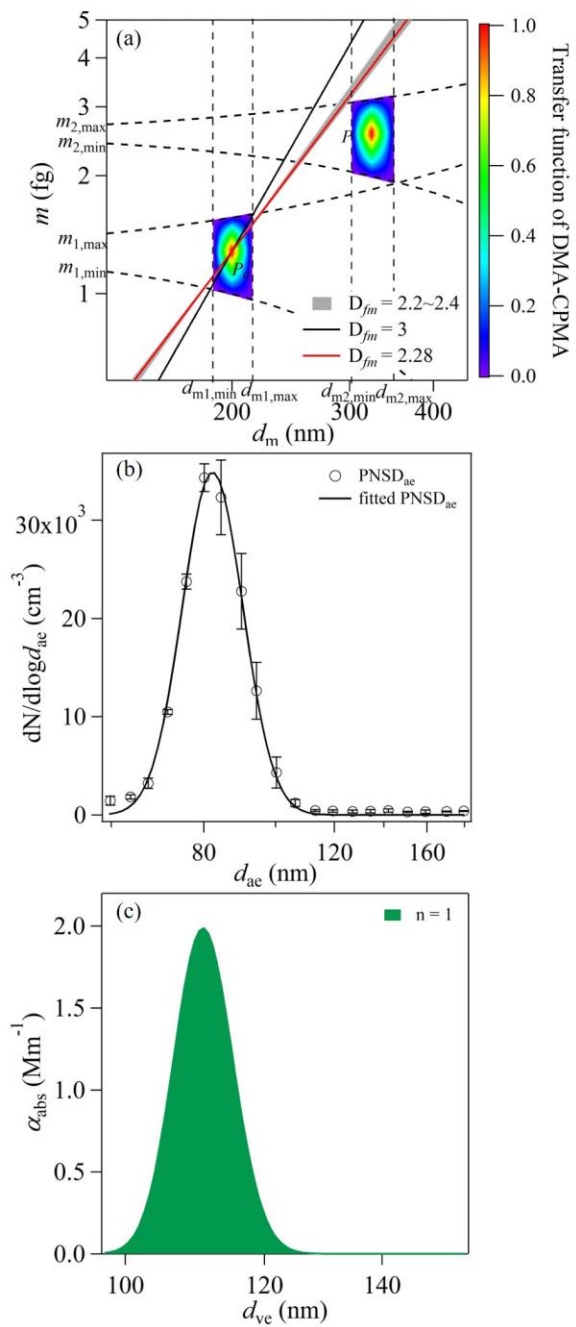
636
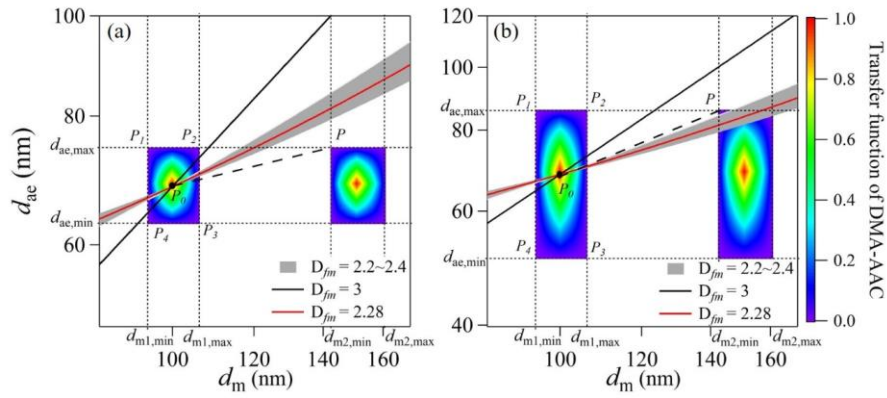
Figure 4: Examples of transfer function calculation of DMA-AAC of flame-generated soot particles (Pei et al., 2018). The following parameter set was employed for the calculations: Q_a=0.3 L min^{-1}, d_{m1} = 100 nm, d_{ae} = 68.3 nm, (a) β_{DMA} = 0.1, β_{AAC} = 0.1, (b) β_{DMA} = 0.1, β_{AAC} = 0.3. The color blocks are the transfer functions of DMA-AAC. The black and red solid lines are particle populations with D_{fm} values of 3 and 2.28, respectively. The gray region is the particles population with D_{fm} of 2.2~2.4, which is typical for soot aerosol. The dashed line is the critical slope of PP$_0$. The dotted lines are the limiting d_m and d_{ae} of DMA and AAC, respectively.

24
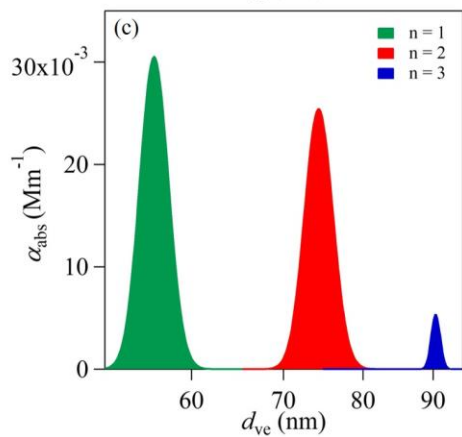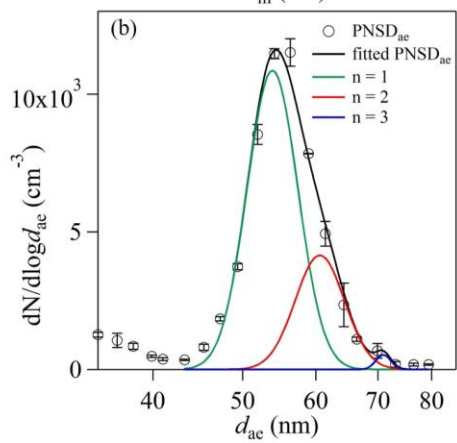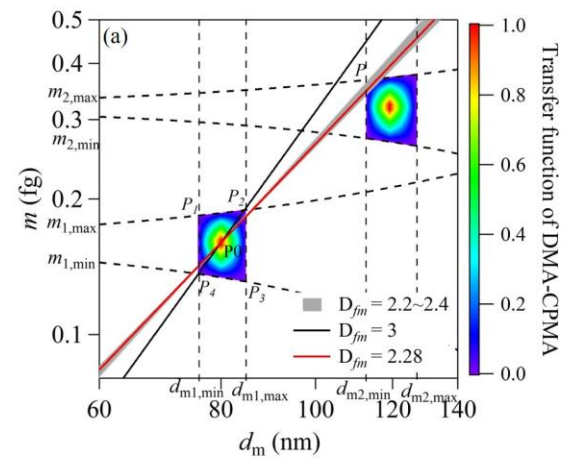
644   **Figure 5: (a) Transfer functions of DMA-CPMA when selecting 80 nm and 0.16 fg particles. The following**
645   **parameter set was employed for the calculations: d_{m1} = 80 nm, β_{DMA} = 0.1, m_1 = 0.16 fg, Q_{CPMA}=0.3 L min^{-1}, R_m =**
646   **8. The red solid line is the generated soot particle population. (b) The aerodynamic size distribution of particles**
647   **classified by DMA-CPMA. The circles are data measured by AAC-CPC, and the black, green, red and blue lines**
648   **are log-normal fitted distributions of bulk, singly charged, doubly charged and triply charged particles**
649   **populations. (c) The contributions to light absorption of particles with single, double and triple charges calculated**
650   **with Mie theory.**

(a)

$m_{2,max}$
$m_{2,min}$

$m_{1,max}$
$m_{1,min}$

P

P

$D_{fm} = 2.2\sim2.4$
$D_{fm} = 3$
$D_{fm} = 2.28$

Transfer function of DMA-CPMA

$d_{m1,min}$ $d_{m1,max}$ $d_{m2,min}$ $d_{m2,max}$

m (fg)

d_m (nm)

(b)

○ PNSD$_{ae}$
— fitted PNSD$_{ae}$

dN/dlogd_{ae} (cm^{-3})

d_{ae} (nm)

(c)

■ n = 1

α_{abs} (Mm^{-1})

d_{ve} (nm)

651

27

652 **Figure 6: (a) The transfer functions of DMA-CPMA when selecting 200 nm and 1.28 fg particles. The following**
653 **parameter set was employed for the calculations: d_{m1} = 200 nm, β_{DMA} = 0.1, m_1 = 1.28 fg, Q_{CPMA}=0.3 L min^{-1}, R_m =**
654 **8. The red solid line is the generated soot particle population. (b) The aerodynamic size distribution of particles**
655 **classified by DMA-CPMA. The circles are data measured by AAC-CPC, and the solid line is the log-normal fitted**
656 **distribution. (c) Contributions to light absorption of particles with a single charge calculated with Mie theory.**

657